

High performance magnesium-based plastic semiconductors for flexible thermoelectrics

Received: 6 April 2024

Accepted: 5 June 2024

Published online: 14 June 2024

 Check for updatesAiran Li^{1,4}, Yuechu Wang^{1,4}, Yuzheng Li^{1,2}, Xinlei Yang¹, Pengfei Nan³, Kai Liu¹, Binghui Ge³, Chenguang Fu¹✉ & Tiejun Zhu^{1,2}✉

Low-cost thermoelectric materials with simultaneous high performance and superior plasticity at room temperature are urgently demanded due to the lack of ever-lasting power supply for flexible electronics. However, the inherent brittleness in conventional thermoelectric semiconductors and the inferior thermoelectric performance in plastic organics/inorganics severely limit such applications. Here, we report low-cost inorganic polycrystalline $\text{Mg}_3\text{Sb}_{0.5}\text{Bi}_{1.498}\text{Te}_{0.002}$, which demonstrates a remarkable combination of large strain (~43%) and high figure of merit zT (~0.72) at room temperature, surpassing both brittle $\text{Bi}_2(\text{Te,Se})_3$ (strain $\leq 5\%$) and plastic $\text{Ag}_2(\text{Te,Se,S})$ and organics ($zT \leq 0.4$). By revealing the inherent high plasticity in Mg_3Sb_2 and Mg_3Bi_2 , capable of sustaining over 30% compressive strain in polycrystalline form, and the remarkable deformability of single-crystalline Mg_3Bi_2 under bending, cutting, and twisting, we optimize the Bi contents in $\text{Mg}_3\text{Sb}_{2-x}\text{Bi}_x$ ($x = 0$ to 1) to simultaneously boost its room-temperature thermoelectric performance and plasticity. The exceptional plasticity of $\text{Mg}_3\text{Sb}_{2-x}\text{Bi}_x$ is further revealed to be brought by the presence of a dense dislocation network and the persistent Mg-Sb/Bi bonds during slipping. Leveraging its high plasticity and strength, polycrystalline $\text{Mg}_3\text{Sb}_{2-x}\text{Bi}_x$ can be easily processed into micro-scale dimensions. As a result, we successfully fabricate both in-plane and out-of-plane flexible $\text{Mg}_3\text{Sb}_{2-x}\text{Bi}_x$ thermoelectric modules, demonstrating promising power density. The inherent remarkable plasticity and high thermoelectric performance of $\text{Mg}_3\text{Sb}_{2-x}\text{Bi}_x$ hold the potential for significant advancements in flexible electronics and also inspire further exploration of plastic inorganic semiconductors.

Thermoelectric (TE) materials have gained significant attention for their ability to convert heat into electricity in a solid-state form¹. With the rapid advancement of flexible electronics², there is a growing demand for TE materials exhibiting both high performance and plasticity at room temperature for reliable and sustainable power

generation^{3,4}. Despite the discovery and development of numerous high-performance TE materials in inorganic semiconductors over the past century, they are inherently brittle⁵. Unlike metallic bonds in metals or polymer chains in organics, the directional covalent bonds in inorganic semiconductors impede atomic layer slipping, leading to

¹State Key Laboratory of Silicon and Advanced Semiconductor Materials, School of Materials Science and Engineering, Zhejiang University, 310058 Hangzhou, China. ²Shanxi-Zheda Institute of Advanced Materials and Chemical Engineering, Taiyuan 030000, China. ³Information Materials and Intelligent Sensing Laboratory of Anhui Province, Key Laboratory of Structure and Functional Regulation of Hybrid Materials of Ministry of Education, Institutes of Physical Science and Information Technology, Anhui University, Hefei 230601, China. ⁴These authors contributed equally: Airan Li, Yuechu Wang.

✉ e-mail: chenguang_fu@zju.edu.cn; zhtj@zju.edu.cn

sudden and unpredictable breakdown under external forces⁶. For instance, commercially available Bi₂Te₃-based compounds typically withstand less than 5% compressive strain before fracturing abruptly^{7,8}. The undesirable brittleness imposes severe limitations on the available processing methods, yield rates, and overall service lifespan of the TE semiconductors, thereby hindering their broader application in various fields, including but not limited to flexible electronics.

In recent years, several inorganic semiconductors with remarkable plasticity have been uncovered, primarily within the chalcogenide systems^{9–15}. Notably, ZnS demonstrates a remarkable 45% compressive strain in darkness⁹, while Ag₂S and its alloys can endure over 10% tensile strain^{10,16–20}. Additionally, van der Waals crystals like InSe¹¹ and SnSe₂²¹ can exhibit obvious flexibility, easily being bent and curved. Compared to organic semiconductors, plastic inorganic semiconductors typically possess superior carrier mobility^{22,23}, making them promising candidates in flexible touch panels²⁴, memristors^{25,26}, and TE generators^{3,27}. However, among these plastic inorganic semiconductors, only Ag₂(Te, Se, S) and SnSe₂ have been reported to exhibit moderate TE performance at room temperature, with a figure of merit ($zT = S^2\sigma T/\kappa$, where S , σ , κ and T represent Seebeck coefficient, electrical conductivity, thermal conductivity, and absolute temperature, respectively) of -0.4 ^{3,8,21}, which are notably higher than that of plastic organic TE materials, but fall significantly short of that in conventional TE compounds. Currently, the absence of materials exhibiting simultaneous high room temperature TE performance and plasticity imposes a significant barrier to the advancement of flexible TE technology.

Low-cost n-type Mg₃Sb_{2-x}Bi_x has attracted significant interest since its discovery due to its impressive high TE performance^{28–31}. Peak zT values of 1.5–1.8 at mid-temperatures (~ 773 K) have been achieved in Mg₃Sb_{2-x}Bi_x with $x = 0.5$ – 1.0 . Apart from its exceptional TE performance, abundant raw materials, high fracture toughness, and good machinability make n-type Mg₃Sb_{2-x}Bi_x highly competitive for future practical applications, particularly at room temperature^{32,33}. Optimizing the Bi content plays a significant role in enhancing the room-temperature performance of Mg₃Sb_{2-x}Bi_x. The synergic effects of reduced bandgap, increased band curvature, strengthened phonon scattering, and enhanced grain size by Bi alloying make Mg₃Sb_{2-x}Bi_x ($x = 1.4$ – 1.75) exhibit zT values above 0.6 at room temperature^{34,35}, which approach to that of the state-of-the-art n-type Bi₂(Te, Se)₃ and are much superior to the plastic Ag₂(Te, Se, S) and organic TE materials^{31,36–39}.

The remarkably high zT values of Mg₃Sb_{2-x}Bi_x have also sparked significant development in its TE modules over the past decades^{40–42}. However, these advancements have predominantly focused on rigid TE modules, neglecting the potential application of Mg₃Sb_{2-x}Bi_x in flexible electronics. Given its notable TE performance and potential plasticity at room temperature³⁶, there exists a compelling opportunity to explore the suitability of Mg₃Sb_{2-x}Bi_x for power generation in flexible electronics. Achieving simultaneous high TE performance and plasticity in Mg₃Sb_{2-x}Bi_x remains a challenge.

In this work, we first focus on binary Mg₃Sb₂ and Mg₃Bi₂, uncovering an exceptionally high compressive strain of >30% in polycrystalline samples. Remarkably, single-crystalline Mg₃Bi₂ also exhibits excellent deformability when subjected to bending, cutting, and twisting. By optimizing the Bi contents to modulate both TE performance and plasticity, a large compressive strain of 43% and a high zT of 0.72 at room temperature are achieved simultaneously in polycrystalline Mg₃Sb_{0.5}Bi_{1.498}Te_{0.002}. The observed dense dislocation network is attributed to facilitating atomic layer slipping in Mg₃Sb_{2-x}Bi_x, while the persistent Mg-Sb/Bi bonds during slipping are crucial for maintaining structural integrity. Additionally, we demonstrate the good machinability of Mg₃Sb_{2-x}Bi_x, which can be processed to unbroken small granules and thin TE legs via dicing and cutting. By assembling thin TE legs on flexible substrates, we have successfully

fabricated both in-plane and out-of-plane flexible modules based on polycrystalline Mg₃Sb_{0.5}Bi_{1.498}Te_{0.002}, showcasing their potential in flexible electronics. The simultaneous high plasticity and high TE performance of Mg₃Sb_{2-x}Bi_x, as well as the demonstration of flexible Mg₃Sb_{2-x}Bi_x TE modules, pave the way for its utilization in flexible electronics and will spur the development of high-performance plastic TE semiconductors.

Results

High TE performance and remarkable plasticity in Mg₃Sb_{2-x}Bi_x

Mg₃Sb_{2-x}Bi_x represents a solid solution combining Mg₃Sb₂ and Mg₃Bi₂. As depicted in Fig. 1a, both polycrystalline Mg₃Sb₂ and Mg₃Bi₂ exhibit remarkable plastic deformation, achieving over 30% strain under uniaxial compression. The optical images inset in Fig. 1a visually demonstrate their high plasticity, where polycrystalline Mg₃Sb₂ can be compressed from 6 mm to 3.6 mm. It should be mentioned that unlike Mg₃Sb₂, which breaks suddenly with a noticeable drop in the stress, Mg₃Bi₂ can be compressed after the first noticeable drop in the stress. The full compressive data for Mg₃Bi₂ is shown in Supplementary Fig. 1, which indicates that Mg₃Bi₂ can be compressed to about 1.6 mm (suggesting a compressive strain of about 80%) after experiencing two noticeable drops in the stress. However, upon examining the optical image of Mg₃Bi₂ after compression, it can be seen that Mg₃Bi₂ bulk shatters into some small pieces. Thus, it is not convincing to take this high compressive strain of 80% as the true compressive performance of Mg₃Bi₂. In addition, polycrystalline Mg₃Sb₂ and Mg₃Bi₂ also exhibit decent tensile strains of about 7.4% and 12.7%, respectively (Supplementary Fig. 2), surpassing numerous inorganic semiconductors and ceramics and even better than plastic Ag₂S (4.2% elongation)¹⁰. The fracture surface morphology of polycrystalline Mg₃Sb₂ and Mg₃Bi₂ after compression is displayed in Supplementary Fig. 3 and Fig. 1b, where the fracture surface of polycrystalline Mg₃Bi₂ exhibits a notable wavy-like characteristic, indicative of its better plasticity and deformability than polycrystalline Mg₃Sb₂. Moreover, it is found that single-crystalline Mg₃Bi₂ in Fig. 1c also demonstrates remarkable deformability, which can be manually bent, twisted and cut, showcasing its potential for flexible electronics, while single-crystalline Mg₃Sb₂ cannot be bent and twisted like single-crystalline Mg₃Bi₂.

While both Mg₃Sb₂ and Mg₃Bi₂ exhibit favorable plasticity, their TE performances, particularly at room temperature, are rather inferior. Bi alloying is rather crucial in optimizing the room temperature zT of Mg₃Sb₂^{30,34}. As shown in Supplementary Fig. 4, Bi alloying has significant impacts on electrical transport properties of Mg₃Sb_{2-x}Bi_x. The downward shift of the peak S in Mg₃Sb_{2-x}Bi_x with higher Bi contents suggests that the bandgap is reduced, in consistency with previous reports^{30–32,34}. Additionally, when Bi content (x) increases to 1.5, there is an obvious rise in room temperature σ , which suggests that the grain boundary scattering is weakened due to the larger grain sizes^{30,34} (fracture morphology of Mg₃Sb_{0.5}Bi_{1.5} in Supplementary Fig. 3). Moreover, Bi alloying leads to lower κ due to the enhanced point defect scattering of phonons. As a result, for polycrystalline Mg₃Sb_{2-x}Bi_x, substantial improvement in room-temperature zT is obtained after increasing the amounts of Bi ($x = 1.5$). A peak zT of 0.72 has been attained at room temperature, while zT values of 0.72–0.86 can be obtained within the near room temperature range (300–478 K) in Mg₃Sb_{0.5}Bi_{1.498}Te_{0.002}, rivaling the commercial high-cost polycrystalline Bi₂(Te,Se)₃. Besides the high TE performance achieved in Mg₃Sb_{2-x}Bi_x, as shown in Fig. 1e, all polycrystalline Mg₃Sb_{2-x}Bi_x samples demonstrate considerable plastic deformation, with compressive strains exceeding 30%, displaying cracks upon finally fracturing. It can also be noticed that the fracture morphology of polycrystalline Bi-rich Mg₃Sb_{2-x}Bi_x ($x = 1.5$) closely resembles that of Mg₃Bi₂ (Supplementary Fig. 3). Notably, polycrystalline Mg₃Sb_{0.5}Bi_{1.498}Te_{0.002} achieves an impressive strain of 43%, overriding the Sb-rich Mg₃Sb_{2-x}Bi_x ($x = 0.5$ and 1). The higher strain of Mg₃Sb_{0.5}Bi_{1.498}Te_{0.002} can be attributed to

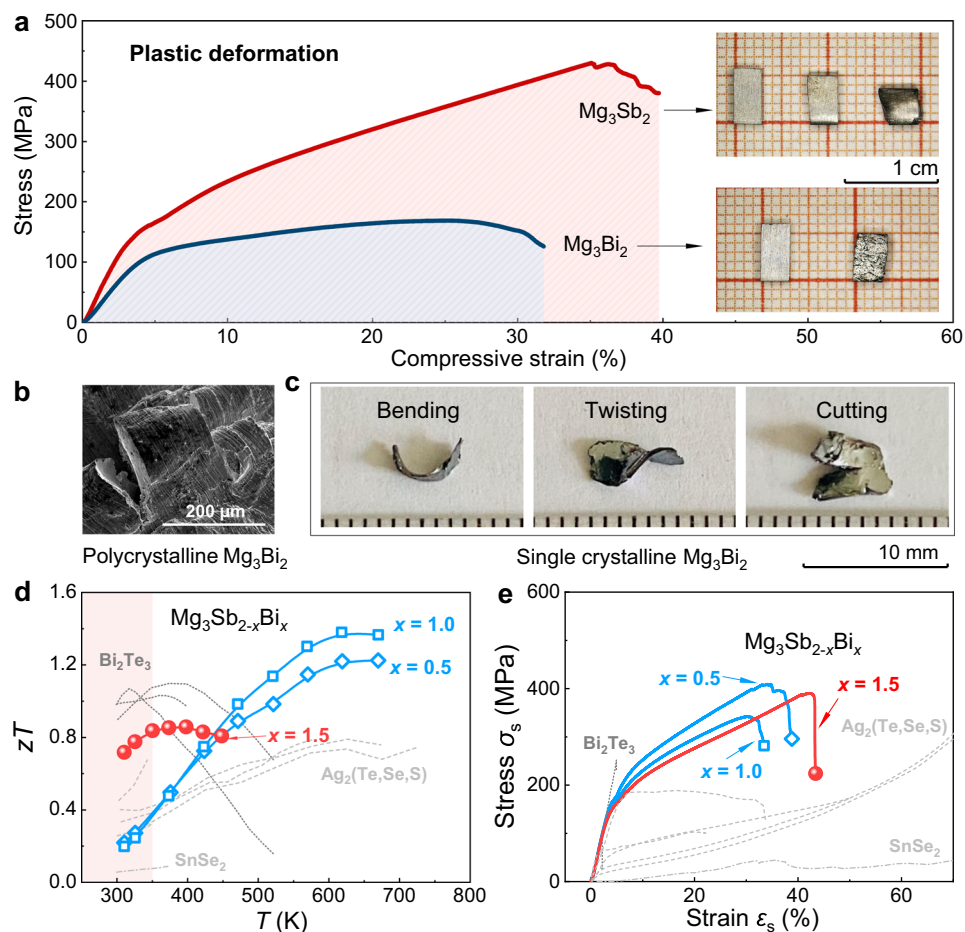


Fig. 1 | The plasticity of $\text{Mg}_3\text{Sb}_{2-x}\text{Bi}_x$. **a** Compressive stress and strain curves of polycrystalline Mg_3Sb_2 and Mg_3Bi_2 with optical images inset showing Mg_3Sb_2 and Mg_3Bi_2 after 33.3% and 16.7% compression, respectively; **b** fracture surface morphology of compressed polycrystalline Mg_3Bi_2 ; **c** optical images of single-

crystalline Mg_3Bi_2 by bending, twisting and cutting; **d** temperature dependence of zT and **e** compressive strain–stress curves of polycrystalline Te-doped $\text{Mg}_3\text{Sb}_{2-x}\text{Bi}_x$, Bi_2Te_3 -based compounds, $\text{Ag}_2(\text{Te,Se,S})$ and SnSe_2 ^{3,7,8,18–21,27,37,58}.

the better plasticity of Mg_3Bi_2 compared to Mg_3Sb_2 as revealed above, which is consistent with the result recently reported⁴³. As a result of the optimized Bi contents, a combination of high plasticity and high TE performance at room temperature has been achieved in low-cost Bi-rich $\text{Mg}_3\text{Sb}_{0.5}\text{Bi}_{1.498}\text{Te}_{0.002}$, which significantly surpasses both commercial $\text{Bi}_2(\text{Te,Se})_3$ (strain $\leq 5\%$), plastic $\text{Ag}_2(\text{Te,Se,S})$ and organic TE materials ($zT \leq 0.4$).

It should be mentioned that Te doping has fewer effects on the plasticity of $\text{Mg}_3\text{Sb}_{2-x}\text{Bi}_x$. As shown in Supplementary Fig. 5, besides the high plasticity of $\text{Mg}_3\text{Sb}_{2-x}\text{Bi}_x$ with Te doping (Fig. 1e), p-type polycrystalline $\text{Mg}_3\text{Sb}_{2-x}\text{Bi}_x$ without doping also exhibits high plasticity (30% compressive strain) across various Sb/Bi ratios. This suggests that plasticity is an inherent characteristic of the $\text{Mg}_3\text{Sb}_{2-x}\text{Bi}_x$ system, and also implies that plasticity is less dependent on electrical transport properties. Therefore, by fine-tuning the carrier concentration and mobility, it is feasible to achieve simultaneous high TE performance and high plasticity in $\text{Mg}_3\text{Sb}_{2-x}\text{Bi}_x$, i.e., the combination of large strain ($\sim 43\%$) and high zT (~ 0.72) achieved in this work via sintering, which is much better than the result reported recently via cold compression⁴³.

Plastic deformation mechanism

Generally, in metals and alloys, dislocations are pivotal in facilitating atomic layer slipping, thus enabling plastic deformation. To reveal the origin of high plasticity in $\text{Mg}_3\text{Sb}_{2-x}\text{Bi}_x$ semiconductors, a microstructure study using the scanning transmission electron microscope (STEM) was conducted. Single-crystalline Mg_3Sb_2 was selected due to

its high resistance against moisture in the air, favorable for efficient microstructure analysis⁴⁴. As shown in Fig. 2a, a notable presence of dislocations can be identified, which will contribute to the high plasticity of Mg_3Sb_2 . During the plastic deformation of Mg_3Sb_2 , the slipping can readily occur owing to the dislocation generation and movement. In addition, an orientation difference can be observed in Mg_3Sb_2 single crystal, which should also contribute to the plasticity by providing an alternative energy-consuming mechanism, akin to twinning- and amorphization-facilitated plastic deformation in high-entropy alloys⁴⁵.

Why do the slipping and dislocations easily occur in Mg_3Sb_2 semiconductors? Recent studies on Ag_2S and other plastic inorganic semiconductors propose small slipping energy or generalized stacking fault energy (GSFE) and large cleavage energy (CE) as criteria for high plasticity¹⁰. In this study, the GSFE and CE of Mg_3Sb_2 and Mg_3Bi_2 have been calculated, as shown in Fig. 2b, c, respectively. Taking Mg_3Sb_2 as an example, both [100](001) and [110](001) directions are identified as probable slipping directions due to their small GSFE values. Considering the crystal symmetry in Mg_3Sb_2 (trigonal crystal structure with $P\bar{3}m1$ space group), there are 8 equivalent slip systems. Moreover, the maximum CE (of -1.4 J m^{-2}) is twice the maximum value of GSFE along these directions (of -0.7 J m^{-2}), indicating ease of slipping but difficulty of cleaving. The abundance of available slip systems, coupled with small GSFE and large CE, contributes to the high plasticity of Mg_3Sb_2 . Similar findings can be confirmed in Mg_3Bi_2 , which also exhibits small GSFE and high CE.

Intrinsically, from a chemical bonding perspective, unlike the delocalized metallic bonds in metals, covalent and ionic bonds typically hinder plastic deformation due to localized electrons. However, in the case of inorganic semiconductors like Mg_3Sb_2 and Mg_3Bi_2 , which both possess covalent bonds according to the charge density difference (CDD) in Supplementary Fig. 6, it is intriguing that they exhibit such high plasticity. Focusing on the [100](001) slipping direction of Mg_3Sb_2 , we calculated the variation of chemical bonding during slipping. As shown in Fig. 2d, CDDs at five different relative displacements (RDs) during slipping were examined, with their corresponding projections on the (001) plane highlighted in the red dashed box. The whole CDDs with RD increasing from 0 to 1 can be found in Supplementary Figs. 7, 8.

Initially (0.0 RD), three bonds exist between Sb and Mg atoms. As RD increased slightly to 0.1, one Mg-Sb bond disappeared quickly, while the other two Mg-Sb bonds can still be observed. Further increasing RD to 0.5 results in only one remaining Mg-Sb bond, with the other two broken. Surprisingly, with a continued increase of RD, new Mg-Sb bonds are sequentially formed until returning to the initial state with three intact bonds. Consequently, despite the breakage of some Mg-Sb bonds during slipping, at least one bond remains within the slipped layers, crucial for maintaining the structural integrity of Mg_3Sb_2 without fracturing during deformation.

To gain a deeper understanding of these persistent bonds between Mg and Sb atoms, we calculated the integrated crystal orbital Hamiltonian population (ICOHP) for Mg1-Sb, Mg2-Sb, and Mg3-Sb bonds. Illustrated in Fig. 2e, as the RD increased, both Mg1-Sb and Mg2-Sb bonds swiftly break, aligning with CDD results in Fig. 2d. However, Mg3-Sb bonds, instead of breakage, undergo continuous strengthening, ensuring the retention of bonding states in the slipped layer. In conventional covalent compounds, directional chemical bonding between slipping layers typically leads to bond breakdown and crack formation during slipping, but the circumstance is quite different for Mg_3Sb_2 . Although Mg1-Sb and Mg2-Sb bonds are broken during deformation, Mg3-Sb bonds persist and even strengthen, which maintains the structural integrity. Similar trends are observed in Mg_3Bi_2 , where Mg1-Bi and Mg2-Bi bonds break while Mg3-Bi bonds persist and strengthen during slipping (Supplementary Figs. 9–11). Consequently, from a chemical bonding perspective, the high plasticity of Mg_3Sb_2 and Mg_3Bi_2 can be attributed to the persistent Mg3-Sb/Bi bonds in the slipped layer, which prevents structural collapse and may also facilitate the dislocation generation and movement, just as the high density of dislocations observed in STEM (Fig. 2a).

High toughness and good machinability in $\text{Mg}_3\text{Sb}_{2-x}\text{Bi}_x$

Synthesized TE materials are typically cut or diced into TE legs, and materials with high toughness can withstand substantial energy, allowing them to be cut or diced into small dimensions with a high yield rate. Toughness can be assessed by the area under the strain-stress curve. Therefore, alongside high plasticity, high strength is also crucial for materials exhibiting high toughness. Figure 3a summarizes both TE and mechanical performances of $\text{Mg}_3\text{Sb}_{0.5}\text{Bi}_{1.498}\text{Te}_{0.002}$, Bi_2Te_3 ⁸, $\text{Ag}_2(\text{Te,S})$ ²⁰ and SnSe_2 ²¹. Among them, polycrystalline $\text{Mg}_3\text{Sb}_{0.5}\text{Bi}_{1.498}\text{Te}_{0.002}$ exhibits high zT , high plasticity (high strain ϵ_s), and high compressive strength σ_s simultaneously at room temperature. This compelling combination of TE and mechanical performance makes polycrystalline $\text{Mg}_3\text{Sb}_{0.5}\text{Bi}_{1.498}\text{Te}_{0.002}$ particularly suitable for room temperature applications, especially considering its low cost. Due to the high strength and plasticity, all polycrystalline $\text{Mg}_3\text{Sb}_{2-x}\text{Bi}_x$ possesses intrinsic high toughness. As shown in Fig. 3b, polycrystalline $\text{Mg}_3\text{Sb}_{0.5}\text{Bi}_{1.498}\text{Te}_{0.002}$ displays simultaneously high TE performance and high toughness at room temperature, making it competitive among the current plastic TE materials.

Due to the high toughness resulting from both high plasticity and strength, polycrystalline $\text{Mg}_3\text{Sb}_{2-x}\text{Bi}_x$ can be diced into small sizes without damage. In contrast, commercial polycrystalline $(\text{Bi,Sb})_2\text{Te}_3$

and $\text{Bi}_2(\text{Te, Se})_3$ fail to be diced much smaller with numerous granules peeled off, as demonstrated in Fig. 3c (detailed dicing images with gradual cut distances from 200 μm to 10 μm can be found in Supplementary Fig. 12). For Mg_3Sb_2 , intact granules with dimensions of about $100 \times 100 \mu\text{m}^2$ and $50 \times 50 \mu\text{m}^2$ can be readily obtained with a high yield rate. $\text{Mg}_3\text{Sb}_{0.5}\text{Bi}_{1.498}\text{Te}_{0.002}$ with superior TE performance can also be effectively diced with the dimension of $100 \times 100 \mu\text{m}^2$. However, diced $(\text{Bi,Sb})_2\text{Te}_3$ and $\text{Bi}_2(\text{Te,Se})_3$ with dimensions of $\sim 150 \times 150 \mu\text{m}^2$ show obvious damaged edges, as shown in Supplementary Fig. 13. Recently, micro-TE devices made of micrometer TE legs have gained much attention, especially for potential applications in 5G communications. The high yield rate of smaller dimension TE legs in $\text{Mg}_3\text{Sb}_{2-x}\text{Bi}_x$ will also benefit its development in micro-TE modules.

Prototype flexible TE modules based on $\text{Mg}_3\text{Sb}_{2-x}\text{Bi}_x$

Due to the high toughness demonstrated above, bulk $\text{Mg}_3\text{Sb}_{2-x}\text{Bi}_x$ can be processed into TE legs with varied and small dimensions (Supplementary Fig. 14) and exhibit possible flexibility if the thickness is thin enough⁴⁶. Considering its high TE performance and high plasticity, thin $\text{Mg}_3\text{Sb}_{2-x}\text{Bi}_x$ TE legs are very suitable to be fabricated as flexible TE modules. Here, we fabricate and demonstrate prototype flexible in-plane (Fig. 4a) and out-of-plane (Fig. 4b) TE modules based on high-performance $\text{Mg}_3\text{Sb}_{0.5}\text{Bi}_{1.498}\text{Te}_{0.002}$. These prototype TE modules are all assembled using flexible polyimide (PI) film bases, Cu conducting wires and $\text{Mg}_3\text{Sb}_{0.5}\text{Bi}_{1.498}\text{Te}_{0.002}$ TE legs.

The in-plane TE module consists of nine n-type $\text{Mg}_3\text{Sb}_{0.5}\text{Bi}_{1.498}\text{Te}_{0.002}$ legs, exhibiting a maximum output voltage V of -6.2 mV and a maximum power density P/A of $-0.24 \mu\text{W}\cdot\text{cm}^{-2}$ when the measured temperature difference of the module ΔT_{module} is -5.6 K (Fig. 4c), where the P is the output power, A is the area of the TE module. Considering the length of the TE legs L , the obtained normalized power density $P \times L/A$ of this in-plane TE module reaches $14.4 \mu\text{W}\cdot\text{m}^{-1}$, significantly surpassing that of PEDOT and Poly[A_x(M-ett)]-based organic flexible TE modules²⁷. However, compared to the state-of-art in-plane flexible TE modules based on $\text{Ag}_2\text{S}_{0.5}\text{Se}_{0.5}$ ²⁷, the performance of this $\text{Mg}_3\text{Sb}_{0.5}\text{Bi}_{1.498}\text{Te}_{0.002}$ flexible TE module is relatively inferior, primarily due to the substantial internal resistance, about 27Ω in $\text{Mg}_3\text{Sb}_{2-x}\text{Bi}_x$ against 9Ω in $\text{Ag}_2\text{S}_{0.5}\text{Se}_{0.5}$ ²⁷. The high internal resistance in $\text{Mg}_3\text{Sb}_{0.5}\text{Bi}_{1.498}\text{Te}_{0.002}$ flexible TE module arises from the significant contact resistance between $\text{Mg}_3\text{Sb}_{0.5}\text{Bi}_{1.498}\text{Te}_{0.002}$ and electrodes. As shown in Supplementary Fig. 15, the contact resistance between $\text{Mg}_3\text{Sb}_{0.5}\text{Bi}_{1.498}\text{Te}_{0.002}$ and Cu electrode is very high, of about $3500 \mu\Omega\cdot\text{cm}^2$. Given the excellent room-temperature zT of plastic $\text{Mg}_3\text{Sb}_{0.5}\text{Bi}_{1.498}\text{Te}_{0.002}$, the reduction of the interfacial resistance of the flexible TE module holds the promise of substantially enhanced performance and fosters future applications in flexible electronics.

In the case of the out-of-plane TE module, it consists of 8 $\text{Mg}_3\text{Sb}_{0.5}\text{Bi}_{1.498}\text{Te}_{0.002}/\text{Cu}$ pairs. A maximum V of 0.3 mV and P/A of $3.9 \text{ nW}\cdot\text{cm}^{-2}$ are achieved with ΔT_{module} of 13.1 K (Fig. 4d). However, it is notable that the performance of the out-of-plane TE module is significantly inferior to that of the in-plane module. This is primarily attributed to the small effective temperature difference ΔT_{leg} established along the thickness direction of TE legs. The ΔT_{leg} can be calculated by using the output voltage of the modules and the Seebeck coefficient of the TE material³. Specifically, the calculated ΔT_{leg} is 3.1 K for the in-plane TE module (with a measured ΔT_{module} of 5.6 K), whereas it is only 0.17 K for the out-of-plane TE module (with a measured ΔT_{module} of 13.1 K). Considering this ΔT_{leg} for the calculation of the normalized power density $P/(A \times \Delta T^2)$ proposed by ref. 3, it reaches $0.13 \mu\text{W}\cdot\text{cm}^{-2}\cdot\text{K}^{-2}$, which surpasses nearly all organic-based flexible TE modules but falls short of Ag_2S -based flexible TE modules³, primarily due to the much higher internal resistance $\sim 7 \Omega$. It is worth mentioning that regardless of whether it is an in-plane or out-of-plane

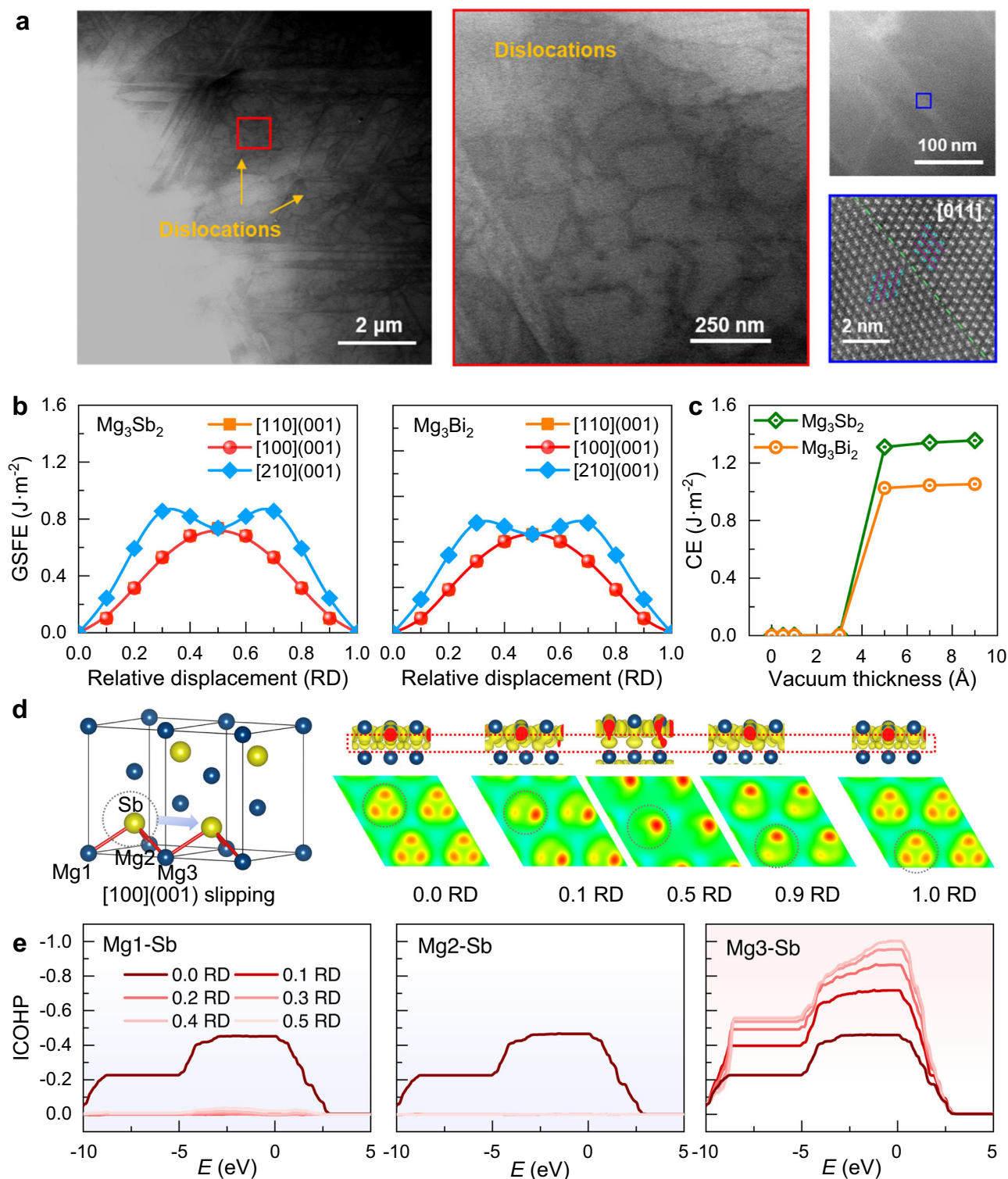


Fig. 2 | The plastic deformation mechanism of $\text{Mg}_3\text{Sb}_{2-x}\text{Bi}_x$. **a** STEM images of single-crystalline Mg_3Sb_2 revealing dislocations and different crystal orientations; **b** the GSFE of Mg_3Sb_2 and Mg_3Bi_2 ; **c** the CE of Mg_3Sb_2 and Mg_3Bi_2 ; **d** the CDDs

between Mg and Sb atoms in the slipped layer; **e** the ICOHPs for Mg1-Sb, Mg2-Sb and Mg3-Sb bonds with different relative displacements RDs.

TE module made of $\text{Mg}_3\text{Sb}_{0.5}\text{Bi}_{1.498}\text{Te}_{0.002}$, the interface between materials and electrodes remains the principal obstacle limiting the module's high performance, despite the materials exhibiting high TE performance. Additionally, in previous Ag-based flexible TE modules, high-performance p-type AgCuSe-based materials were used³. This also suggests possible ways to future improve the output performance

of $\text{Mg}_3\text{Sb}_{2-x}\text{Bi}_x$ flexible modules if high-performance p-type Mg-based TE materials are developed. Optimization of the interface, such as using appropriate interface materials^{47,48}, and advancement of high-performance p-type plastic TE materials hold promise for achieving significantly better performance of the flexible TE module based on $\text{Mg}_3\text{Sb}_{2-x}\text{Bi}_x$.

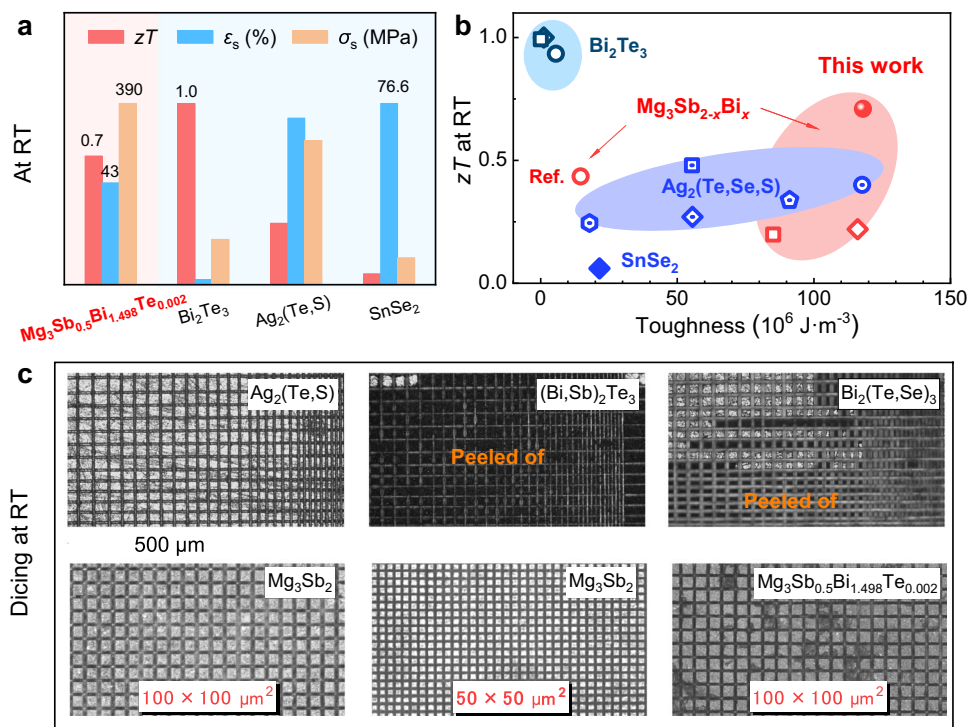


Fig. 3 | The mechanical performance, TE performance and machinability of polycrystalline $\text{Mg}_3\text{Sb}_{2-x}\text{Bi}_x$. **a** The summarized zT , ϵ_s and σ_s of $\text{Mg}_3\text{Sb}_{0.5}\text{Bi}_{1.498}\text{Te}_{0.002}$, Bi_2Te_3 -based compounds⁸, $\text{Ag}_2(\text{Te,S})$ ²⁰ and SnSe_2 ²¹ at room

temperature; **b** the room temperature zT vs. toughness in $\text{Mg}_3\text{Sb}_{2-x}\text{Bi}_x$, Bi_2Te_3 -based compounds, $\text{Ag}_2(\text{Te,Se,S})$ and SnSe_2 ^{3,7,8,18–21,27,37,58}; **c** the optical images of diced $\text{Ag}_2(\text{Te,S})$, $(\text{Bi,Sb})_2\text{Te}_3$, $\text{Bi}_2(\text{Te,Se})_3$, Mg_3Sb_2 and $\text{Mg}_3\text{Sb}_{0.5}\text{Bi}_{1.498}\text{Te}_{0.002}$.

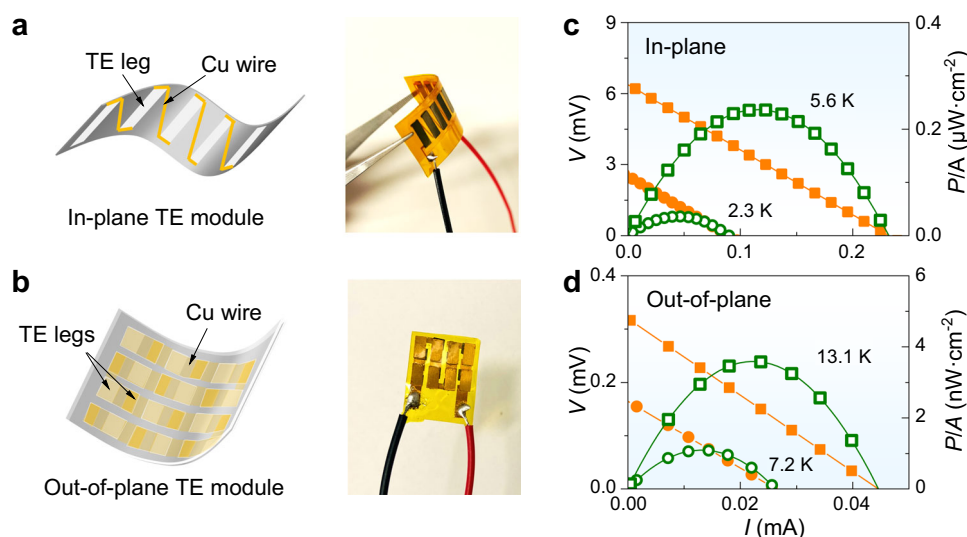


Fig. 4 | The in-plane and out-of-plane TE modules of $\text{Mg}_3\text{Sb}_{2-x}\text{Bi}_x$. The fabricated (a) in-plane and (b) out-of-plane TE module based on $\text{Mg}_3\text{Sb}_{0.5}\text{Bi}_{1.498}\text{Te}_{0.002}$ with its schematics on the left; the output voltage V and power density P/A of (c) in-plane

and (d) out-of-plane TE modules. The temperature value is the temperature difference of the module ΔT_{module} .

Discussion

In this study, the inherent high plasticity of Mg_3Sb_2 and Mg_3Bi_2 has been revealed. Despite intrinsic covalent/ionic bonding, polycrystalline Mg_3Sb_2 and Mg_3Bi_2 hold over 30% compressive strain. By optimizing the Bi contents, compressive strain $\sim 43\%$ and $zT \sim 0.72$ can be achieved simultaneously in Bi-rich polycrystalline $\text{Mg}_3\text{Sb}_{0.5}\text{Bi}_{1.498}\text{Te}_{0.002}$ at room temperature, surpassing the room temperature performance of known plastic TE semiconductors. The persistent Mg-Sb/Bi bonds within the slipped layer, along with the abundance of dislocations, are revealed as important contributors to

the high plasticity of $\text{Mg}_3\text{Sb}_{2-x}\text{Bi}_x$, ensuring structural integrity maintenance and facilitating atomic layer slipping during deformation, respectively.

Furthermore, the high toughness resulting from the high plasticity and strength enables polycrystalline $\text{Mg}_3\text{Sb}_{2-x}\text{Bi}_x$ to be easily diced into granules below $100 \times 100 \mu\text{m}^2$ without edge damage and cut into TE legs of various dimensions. Both in-plane and out-of-plane flexible TE modules based on polycrystalline $\text{Mg}_3\text{Sb}_{0.5}\text{Bi}_{1.498}\text{Te}_{0.002}$ have been assembled and demonstrated, exhibiting much higher performance compared to organic-based flexible TE modules with promising

opportunities for further enhancement by reducing the interface resistance. The revealed intrinsically high plasticity, high TE performance as well as good machinability in polycrystalline $\text{Mg}_3\text{Sb}_{2-x}\text{Bi}_x$ will advance their potential applications in flexible electronics.

Methods

Materials synthesis

$\text{Mg}_3\text{Sb}_{2-x}\text{Bi}_x$ and $\text{Mg}_3\text{Sb}_{2-x}\text{Bi}_{x-y}\text{Te}_y$ ($x = 0.5, 1.0, 1.5; y = 0.002, 0.01, 0.02$) were synthesized by mechanical alloying with 10% excessive Mg contents. Mg powders (99.8%), Sb powders (99.9%), Bi powders (99.9%) and/or Te powders (99.999%) were used and weighed in the glove box, and then mechanically alloyed for 2 h (SPEX-8000D, PYNM). The obtained powder products were solidated by vacuum spark plasma sintering (LABOX-650F, Sinter Land Inc.) under 973 K and 60 MPa for 2 min. The relative density of all sintered samples reaches above 97%. The single-crystalline Mg_3Sb_2 and Mg_3Bi_2 were grown by self-flux method with excess Sb/Bi^{44,49}. The $\text{Ag}_2(\text{Te},\text{S})$ used for dicing tests were obtained by melting method. High-purity Ag shots (99.999%), Te shots (99.999%), and S flakes (99.999%) were used and weighted accordingly, which were then loaded and sealed in the quartz tube for the melting at 1273 K⁹, and the commercial $\text{Bi}_2(\text{Te},\text{Se})_3$ and $(\text{Bi},\text{Sb})_2\text{Te}_3$ were produced by hot extrusion.

Characterization and measurements

The compressed fracture surface morphology was investigated by the SEM (Hitachi, S-3400N). The microstructures of Mg_3Sb_2 single crystal were studied by high-resolution STEM (Cs corrected JEOL ARM 200F microscope). The TE performance zT of $\text{Mg}_3\text{Sb}_{2-x}\text{Bi}_{x-y}\text{Te}_y$ was calculated by the formula: $zT = S^2\sigma T/\kappa$, in which the S and the σ were measured by Linseis LSR-3 system with measurement uncertainties of S and σ about $\pm 5\%$ and $\pm 3\%$, respectively, and the κ was calculated by the formula: $\kappa = D\rho C_p$, where the thermal diffusivity D was measured by Netzsch LFA457 with about $\pm 3\%$ uncertainty, the sample density ρ was estimated by the Archimedes method, and heat capacity C_p was calculated according to a previous study⁵⁰. The calculated uncertainty of zT is within $\pm 10\%$. Compressive tests of cuboids ($3 \times 3 \times 6 \text{ mm}^3$) and tensile tests of plates ($3 \times 0.7 \times 27 \text{ mm}^3$) were performed by a universal testing machine (Siomm, JVI-20S, China) under a loading rate of $1 \text{ mm}\cdot\text{min}^{-1}$. The experiments of dicing were carried out by using a commercialized dicing machine (Qisheng-D0620, China) with a spindle speed of about 30,000 rpm and a dicing speed of 0.3 mm/s. The dicing did not cut the ingot thoroughly, which allowed the cut blocks to remain attached to the original ingot. Two types of cutting programs have been used. The first is a regular cut, where the ingot is cut into blocks of $150 \times 150 \mu\text{m}^2$, $100 \times 100 \mu\text{m}^2$ or $50 \times 50 \mu\text{m}^2$. The second is a gradual cut, where the cut distance decreases in every two cut steps: 200 μm , 150 μm , 100 μm , 50 μm , 20 μm , and finally 10 μm .

Module fabrication and test

High-performance $\text{Mg}_3\text{Sb}_{0.5}\text{Bi}_{1.498}\text{Te}_{0.002}$ TE legs with dimensions of $1.8 \times 0.12 \times 6 \text{ mm}^3$ and $1.8 \times 1.8 \times 0.12 \text{ mm}^3$ were used for fabricating in-plane and out-of-plane TE modules, respectively. The thickness of $\text{Mg}_3\text{Sb}_{0.5}\text{Bi}_{1.498}\text{Te}_{0.002}$ TE legs is first reduced by cutting to 0.5 mm and then by manually polishing to 0.12 mm. PI films and Cu sheets were used as support bases and conducting wires. High conductive Ag pastes were used to connect TE legs and Cu wires. Contact resistance between $\text{Mg}_3\text{Sb}_{0.5}\text{Bi}_{1.498}\text{Te}_{0.002}$ and Cu joint was measured by using a home-build instrument⁵¹. A home-build instrument with a source meter (K2400, Keithley) was used to measure the output voltage and source current of the TE modules. The temperature gradient is applied along the length direction in the in-plane module and thickness direction in the out-of-plane module by one-side heating and the other-side cooling. Two K-type thermocouples were used to record the temperatures of the hot and cold sides of the module, respectively. ΔT_{module} was obtained by the differences of the temperatures

measured by the two thermocouples, while ΔT_{leg} was calculated by using the output voltage of the modules and the Seebeck coefficient of the TE material³.

First-principles calculations

First-principles calculations were performed by the software Vienna ab initio Simulation Package (VASP) with the projector augmented-wave method based on density functional theory^{52,53}. Generalized gradient approximation - Perdew-Burke-Ernzerhof type (GGA-PBE) and modified Becke-Johnson were used as the exchange-correlation functionals^{54,55}. Plane-wave energy cutoff, Hellmann-Feynman force on each atom energy and convergence criterion were set as 500 eV, $0.001 \text{ eV}\cdot\text{\AA}^{-1}$ and 10^{-8} eV , respectively. Geometry relaxation and self-consistent static calculations adopted the Gamma-centered k -point sampling with $k = 30/L$ and $60/L$, respectively, where the L is the corresponding lattice parameter. The GSFE and CE were calculated based on the $2 \times 2 \times 4$ supercell. To analyze the GSFE, $2 \times 2 \times 2$ half of the supercell is artificially shifted along a specific crystallographic direction at 10-step RDs. For CE analysis, a vacuum layer with varied thickness is inserted into the half of the supercell to simulate the artificial separation of the crystal into two parts. VASPKIT⁵⁶ and Lobster⁵⁷ have been used to post-process the calculated data, including CDD and ICOHP.

Data availability

All data generated or analyzed during this study are included in this published article (and its supplementary information file).

References

- He, J. & Tritt, T. M. Advances in thermoelectric materials research: Looking back and moving forward. *Science* **357**, eaak9997 (2017).
- Sanderson, K. Electronic skin: from flexibility to a sense of touch. *Nature* **591**, 685–687 (2021).
- Yang, Q. et al. Flexible thermoelectrics based on ductile semiconductors. *Science* **377**, 854–858 (2022).
- Nan, K. et al. Compliant and stretchable thermoelectric coils for energy harvesting in miniature flexible devices. *Sci. Adv.* **4**, eaau5849 (2018).
- Hou, C. & Zhu, M. Semiconductors flex thermoelectric power. *Science* **377**, 815–816 (2022).
- Schoeck, G. *Advances in Applied Mechanics*, Vol. **4** (eds H. L. Dryden & Th von Kármán) 229–279 (Elsevier, 1956).
- Zhu, Y.-K. et al. Mediating point defects endows n-type Bi_2Te_3 with high thermoelectric performance and superior mechanical robustness for power generation application. *Small* **18**, 2201352 (2022).
- Qiu, J. et al. 3D printing of highly textured bulk thermoelectric materials: mechanically robust BiSbTe alloys with superior performance. *Energy Environ. Sci.* **12**, 3106–3117 (2019).
- Oshima, Y., Nakamura, A. & Matsunaga, K. Extraordinary plasticity of an inorganic semiconductor in darkness. *Science* **360**, 772–774 (2018).
- Shi, X. et al. Room-temperature ductile inorganic semiconductor. *Nat. Mater.* **17**, 421–426 (2018).
- Wei, T.-R. et al. Exceptional plasticity in the bulk single-crystalline van der Waals semiconductor InSe . *Science* **369**, 542–545 (2020).
- Zhang, J. et al. Plastic deformation in silicon nitride ceramics via bond switching at coherent interfaces. *Science* **378**, 371–376 (2022).
- Gao, Z. et al. High-throughput screening of 2D van der Waals crystals with plastic deformability. *Nat. Commun.* **13**, 7491 (2022).
- Wu, Y. et al. Twisted-layer boron nitride ceramic with high deformability and strength. *Nature* **626**, 779–784 (2024).
- Li, X. et al. Multislip-enabled morphing of all-inorganic perovskites. *Nat. Mater.* **22**, 1175–1181 (2023).

16. Yang, S. et al. Ductile $\text{Ag}_{20}\text{S}_7\text{Te}_3$ with excellent shape-conformability and high thermoelectric performance. *Adv. Mater.* **33**, 2007681 (2021).
17. Gao, Z. et al. p-Type plastic inorganic thermoelectric materials. *Adv. Energy Mater.* **11**, 2100883 (2021).
18. He, S. et al. Semiconductor glass with superior flexibility and high room temperature thermoelectric performance. *Sci. Adv.* **6**, eaaz8423 (2020).
19. Wang, Y., Li, A., Hu, H., Fu, C. & Zhu, T. Reversible room temperature brittle-plastic transition in $\text{Ag}_2\text{Te}_{0.6}\text{S}_{0.4}$ inorganic thermoelectric semiconductor. *Adv. Funct. Mater.* **33**, 2300189 (2023).
20. Hu, H., Wang, Y., Fu, C., Zhao, X. & Zhu, T. Achieving metal-like malleability and ductility in $\text{Ag}_2\text{Te}_{1-x}\text{S}_x$ inorganic thermoelectric semiconductors with high mobility. *Innovation* **3**, 100341 (2022).
21. Deng, T. et al. Plastic/ductile bulk 2D van der Waals single-crystalline SnSe_2 for flexible thermoelectrics. *Adv. Sci.* **9**, 2203436 (2022).
22. Wang, Y. et al. Flexible thermoelectric materials and generators: challenges and innovations. *Adv. Mater.* **31**, 1807916 (2019).
23. Wei, T.-R., Qiu, P., Zhao, K., Shi, X. & Chen, L. Ag_2Q -based (Q = S, Se, Te) silver chalcogenide thermoelectric materials. *Adv. Mater.* **35**, 2110236 (2023).
24. Zhao, X.-F. et al. A fully flexible intelligent thermal touch panel based on intrinsically plastic Ag_2S semiconductor. *Adv. Mater.* **34**, 2107479 (2022).
25. Zhu, Y., Liang, J.-s., Shi, X. & Zhang, Z. Full-inorganic flexible Ag_2S memristor with interface resistance-switching for energy-efficient computing. *ACS Appl. Mater. Interfaces* **14**, 43482–43489 (2022).
26. Jo, S. et al. Solution-processed stretchable Ag_2S semiconductor thin films for wearable self-powered nonvolatile memory. *Adv. Mater.* **33**, 2100066 (2021).
27. Liang, J. et al. Flexible thermoelectrics: from silver chalcogenides to full-inorganic devices. *Energy Environ. Sci.* **12**, 2983–2990 (2019).
28. Tamaki, H., Sato, H. K. & Kanno, T. Isotropic conduction network and defect chemistry in $\text{Mg}_{3+\delta}\text{Sb}_2$ -based layered zintl compounds with high thermoelectric performance. *Adv. Mater.* **28**, 10182–10187 (2016).
29. Zhang, J. et al. Discovery of high-performance low-cost n-type Mg_3Sb_2 -based thermoelectric materials with multi-valley conduction bands. *Nat. Commun.* **8**, 13901 (2017).
30. Imasato, K., Kang, S. D. & Snyder, G. J. Exceptional thermoelectric performance in $\text{Mg}_3\text{Sb}_{0.6}\text{Bi}_{1.4}$ for low-grade waste heat recovery. *Energy Environ. Sci.* **12**, 965–971 (2019).
31. Shu, R. et al. $\text{Mg}_{3+\delta}\text{Sb}_x\text{Bi}_{2-x}$ family: a promising substitute for the state-of-the-art n-type thermoelectric materials near room temperature. *Adv. Funct. Mater.* **29**, 1807235 (2019).
32. Mao, J. et al. High thermoelectric cooling performance of n-type Mg_3Bi_2 -based materials. *Science* **365**, 495–498 (2019).
33. Zhang, F. et al. High-performance N-type Mg_3Sb_2 towards thermoelectric application near room temperature. *Adv. Funct. Mater.* **30**, 1906143 (2020).
34. Li, A., Fu, C., Zhao, X. & Zhu, T. High-performance $\text{Mg}_3\text{Sb}_{2-x}\text{Bi}_x$ thermoelectrics: progress and perspective. *Research* **2020**, 1934848 (2020).
35. Wang, L. et al. Realizing high thermoelectric performance in N-Type $\text{Mg}_3(\text{Sb}, \text{Bi})_2$ -based materials via synergetic Mo addition and Sb–Bi Ratio Refining. *Adv. Energy Mater.* **13**, 2301667 (2023).
36. Li, J. et al. Point defect engineering and machinability in n-type Mg_3Sb_2 -based materials. *Mater. Today Phys.* **15**, 100269 (2020).
37. Lei, J. et al. Efficient lanthanide Gd doping promoting the thermoelectric performance of Mg_3Sb_2 -based materials. *J. Mater. Chem. A* **9**, 25944–25953 (2021).
38. Jiang, F. et al. Extraordinary thermoelectric performance, thermal stability and mechanical properties of n-type $\text{Mg}_3\text{Sb}_{1.5}\text{Bi}_{0.5}$ through multi-dopants at interstitial site. *Mater. Today Phys.* **27**, 100835 (2022).
39. Wan, C. et al. Flexible n-type thermoelectric materials by organic intercalation of layered transition metal dichalcogenide TiS_2 . *Nat. Mater.* **14**, 622–627 (2015).
40. Liu, Z. et al. Demonstration of ultrahigh thermoelectric efficiency of $\sim 7.3\%$ in $\text{Mg}_3\text{Sb}_2/\text{MgAgSb}$ module for low-temperature energy harvesting. *Joule* **5**, 1196–1208 (2021).
41. Liu, Z. et al. Maximizing the performance of n-type Mg_3Bi_2 -based materials for room-temperature power generation and thermoelectric cooling. *Nat. Commun.* **13**, 1120 (2022).
42. Ying, P. et al. Towards tellurium-free thermoelectric modules for power generation from low-grade heat. *Nat. Commun.* **12**, 1121 (2021).
43. Zhang, Z. et al. Plastic $\text{Mg}_3(\text{Sb}, \text{Bi})_2$ -based thermoelectric compounds with enhanced texture via cold-deformation. *J. Mater. Chem. A* **12**, 8893–8899 (2024).
44. Li, A. et al. Chemical stability and degradation mechanism of $\text{Mg}_3\text{Sb}_{2-x}\text{Bi}_x$ thermoelectrics towards room-temperature applications. *Acta Mater.* **239**, 118301 (2022).
45. Zhao, S. et al. Amorphization in extreme deformation of the CrMnFeCoNi high-entropy alloy. *Sci. Adv.* **7**, eabb3108 (2021).
46. Peng, J. & Snyder, G. J. A figure of merit for flexibility. *Science* **366**, 690–691 (2019).
47. Yin, L. et al. Low-temperature sintering of Ag nanoparticles for high-performance thermoelectric module design. *Nat. Energy* **8**, 665–674 (2023).
48. Xie, L. et al. Screening strategy for developing thermoelectric interface materials. *Science* **382**, 921–928 (2023).
49. Nan, P. et al. Visualizing the Mg atoms in Mg_3Sb_2 thermoelectrics using advanced iDPC-STEM technique. *Mater. Today Phys.* **21**, 100524 (2021).
50. Agne, M. T. et al. Heat capacity of Mg_3Sb_2 , Mg_3Bi_2 , and their alloys at high temperature. *Mater. Today Phys.* **6**, 83–88 (2018).
51. Xiong, B. et al. Low interfacial resistivity in $\text{CoSi}_2/\text{ZrCoSb}$ thermoelectric junctions. *Mater. Today Energy* **25**, 100960 (2022).
52. Kresse, G. & Furthmüller, J. Efficient iterative schemes for ab initio total-energy calculations using a plane-wave basis set. *Phys. Rev. B* **54**, 11169–11186 (1996).
53. Kresse, G. & Joubert, D. From ultrasoft pseudopotentials to the projector augmented-wave method. *Phys. Rev. B* **59**, 1758–1775 (1999).
54. Perdew, J. P., Burke, K. & Ernzerhof, M. Generalized gradient approximation made simple. *Phys. Rev. Lett.* **77**, 3865–3868 (1996).
55. Tran, F. & Blaha, P. Accurate band gaps of semiconductors and insulators with a semilocal exchange-correlation potential. *Phys. Rev. Lett.* **102**, 226401 (2009).
56. Wang, V., Xu, N., Liu, J.-C., Tang, G. & Geng, W.-T. VASPKit: A user-friendly interface facilitating high-throughput computing and analysis using VASP code. *Comput. Phys. Commun.* **267**, 108033 (2021).
57. Dronskowski, R. & Bloechl, P. E. Crystal orbital Hamilton populations (COHP): energy-resolved visualization of chemical bonding in solids based on density-functional calculations. *J. Phys. Chem.* **97**, 8617–8624 (1993).
58. Zheng, Y. et al. High-temperature mechanical and thermoelectric properties of p-Type $\text{Bi}_{0.5}\text{Sb}_{1.5}\text{Te}_3$ commercial zone melting ingots. *J. Electron. Mater.* **43**, 2017–2022 (2014).

Acknowledgements

This work was supported by the National Key Research and Development Program of China (No. 2023YFB3809400, T.Z.), the National Natural Science Foundation of China (No. U23A20553, T.Z.; No. 92163203, T.Z.; No. 52101275, C.F.), the Fundamental Research Funds for the Zhejiang Provincial Universities (No. 226-2023-00001, C.F.).

Author contributions

A.L., C.F. and T.Z. designed the project. A.L. and Y.W. prepared the samples and carried out the transport measurements, mechanical tests and first-principles calculations. Y.W., Y.L. and X.Y. provided the samples of $\text{Ag}_2(\text{Te,S})$, $\text{Bi}_2(\text{Te,Se})_3$ and $(\text{Bi,Sb})_2\text{Te}_3$. P.N. and B.G. carried out the scanning transmission electron microscopy study. A.L. fabricated the flexible thermoelectric modules and measured the performance with input from K.L. A.L. analyzed the data and wrote the original manuscript with input from Y.W. and C.F. C.F. and T.Z. supervised the whole project. All the authors reviewed and edited the manuscript.

Competing interests

The authors declare no competing interests.

Additional information

Supplementary information The online version contains supplementary material available at <https://doi.org/10.1038/s41467-024-49440-5>.

Correspondence and requests for materials should be addressed to Chenguang Fu or Tiejun Zhu.

Peer review information *Nature Communications* thanks Chengyi Hou, Longlu Wang and the other anonymous reviewer(s) for their contribution to the peer review of this work. A peer review file is available.

Reprints and permissions information is available at <http://www.nature.com/reprints>

Publisher's note Springer Nature remains neutral with regard to jurisdictional claims in published maps and institutional affiliations.

Open Access This article is licensed under a Creative Commons Attribution 4.0 International License, which permits use, sharing, adaptation, distribution and reproduction in any medium or format, as long as you give appropriate credit to the original author(s) and the source, provide a link to the Creative Commons licence, and indicate if changes were made. The images or other third party material in this article are included in the article's Creative Commons licence, unless indicated otherwise in a credit line to the material. If material is not included in the article's Creative Commons licence and your intended use is not permitted by statutory regulation or exceeds the permitted use, you will need to obtain permission directly from the copyright holder. To view a copy of this licence, visit <http://creativecommons.org/licenses/by/4.0/>.

© The Author(s) 2024